

Article

Synergistic Effect of Nonthermal Plasma and ZnO Nanoparticles on Organic Dye Degradation

E. Abdel-Fattah ^{1,2,*}  and S. Alotibi ¹ 

¹ Department of Physics, College of Science and Humanities, Prince Sattam Bin Abdulaziz University, Al-Kharj 11942, Saudi Arabia; sf.alotibi@psau.edu.sa

² Physics Department, Faculty of Science, Zagazig University, Zagazig 44519, Egypt

* Correspondence: e.abdelfattah@psau.edu.sa

Abstract: The synergetic effect of nonthermal plasma and ZnO nanoparticles (NPs) on the degradation efficiency of methylene blue was investigated. First, the ZnO nanoparticles were synthesized via the hydrothermal route; the spherical nanoparticles had diameters of 30–50 nm, as observed with a scanning electron microscope (SEM), and had hexagonal ZnO lattice structures, which was confirmed by both X-ray diffraction (XRD) and Raman spectroscopy. The X-ray-photoemission spectroscopy confirmed the ZnO composition and the presence of oxygen vacancies; meanwhile, the optical band gap energy was 3.17 eV. The optical emission of plasma radiation confirmed the presence of various active plasma species. Second, it was found that the maximum degradation efficiency of MB after 60 min was 85% in plasma alone and increased to 95% when combined with 0.2 gL⁻¹ ZnO; but this decreased to 75% when ZnO loading increased to 0.4 gL⁻¹. These results clearly show that combining plasma with the right amount of ZnO is a promising advanced oxidation technique as it provides an additional source of hydroxyl radicals and, at the same time, a source of photons that can excite the ZnO catalyst. The degradation mechanism for plasma alone and the plasma in combination with ZnO was presented.

Keywords: nonthermal plasma; ZnO nanoparticles; methylene blue degradation; XPS; XRD; OES; Raman



Citation: Abdel-Fattah, E.; Alotibi, S. Synergistic Effect of Nonthermal Plasma and ZnO Nanoparticles on Organic Dye Degradation. *Appl. Sci.* **2023**, *13*, 10045. <https://doi.org/10.3390/app131810045>

Academic Editor: Paolo Proposito

Received: 6 August 2023

Revised: 25 August 2023

Accepted: 29 August 2023

Published: 6 September 2023



Copyright: © 2023 by the authors. Licensee MDPI, Basel, Switzerland. This article is an open access article distributed under the terms and conditions of the Creative Commons Attribution (CC BY) license (<https://creativecommons.org/licenses/by/4.0/>).

1. Introduction

The widespread use of organic dyes in various industries, such as textiles, cosmetics, and printing, has led to significant environmental problems due to the discharge of wastewater-containing dyes [1]. These dyes can be toxic and persistent, pose a threat to aquatic ecosystems, and potentially affect human health if they enter the water supplies [2–4]. Methylene blue (MB), C₁₆H₁₈N₃SCl, is a synthetic dye used in the textile industry to dye fabrics. Its discharge has effects on aquatic life and human health [5]. Therefore, the development of efficient and environmentally friendly techniques for dye degradation and the removal of dyes is indeed a challenging task [6–10].

A variety of dye degradation methods have been developed, such as biodegradation and biotransformation, which utilize microorganisms to degrade organic dyes [11,12], an adsorption technique using natural or synthetic materials that adsorb and remove organic dyes from wastewater [13], and reverse osmosis and an ultra-filtration membrane [14,15]. Though the biological method is low-cost, it is doubtful whether it degrades MB completely in water [16] and it generates a large amount of sludge, affecting the ecological system [12]. Meanwhile, adsorption and ultra-filtration approaches face challenges such as the regeneration of the adsorbent for re-usability and membrane fouling and high energy consumption, respectively. Other approaches for wastewater treatment are based on the generation and usage of oxidants, such as photocatalysis, in which a semiconductor nanostructure is illuminated with UV-Vis and, hence, generates oxidants that interact with the dye molecule [17]. The Fenton reaction involves Fe²⁺ ions interacting with H₂O and

producing hydroxyl radicals, OH [18]. The advanced oxidation process employs H₂O₂, ozone (O₃), and/or UV light to enhance hydroxyl radicals' production [19].

Plasma is a partially ionized gas containing various reactive species, including ions, radicals, and excited molecules. Its versatile chemical compositions enable its strong oxidizing and/or reducing properties, making them effective tools for organic dye degradation. The atmospheric-pressure plasma jet (APPJ) generates a plasma plume in open air. The plasma plume is composed of various reactive species and emits photons with a wide spectral range. The APPJ has received increasing attention due to its great potential for a variety of applications in nanotechnology, surface engineering, and material processing [20–23]. Plasma technology has been shown to be a promising approach for the degradation of organic dyes [24], which has the advantages of having a short treatment time, being chemical-free, and leaving no residuals behind. However, there are several limitations associated with the plasma treatment of dyes, such as the lack of selectivity, higher energy consumption, limited penetration depth, and scalability. One possible strategy to improve plasma performance in dye degradation is to combine plasma with metal oxide nanomaterials. Photocatalytic studies of various photocatalysts combined with plasma have been investigated. Lin et al. synthesized a novel photocatalyst and combined it with dielectric barrier discharge (DBD) plasma to remove isopropanol (IPA) [25]. Jia et al. studied the mineralization of toluene using nonthermal plasma combined with CeO₂ as an adsorbent and found that the amount of ozone produced by the discharge plays a key role in the mineralization process [26]. The combination of plasma with nanomaterials could improve the generation of reactive species and the reaction area and increase the selectivity of the degradation process [27–30].

Zinc oxide nanoparticles ZnO have attracted much attention in environmental remediation due to their unique properties, such as large surface area, photocatalytic activity, and stability [31]. The degradation efficiency of ZnO nanoparticles alone can sometimes be limited, especially for dyes that are resistant to degradation or have complex molecular structures. The combination of plasma and ZnO nanoparticles is a promising approach for the degradation of organic dyes. Plasma generates reactive species that further oxidize and degrade the organic dye molecules [24]. Further, plasma can activate the ZnO nanoparticles, enhancing their photocatalytic activity and accelerating the degradation process. This innovative technology provides an environmentally friendly solution to increasing dye pollution. However, the exact mechanism of how plasma enhances the performance of ZnO nanoparticles in organic dye degradation is not fully understood and can vary depending on the specific experimental conditions and parameters used.

In summary, we investigated the synergistic effects of nonthermal plasma and ZnO on the efficiency of MB dye degradation. We synthesized ZnO NPs via the hydrothermal method and then characterized them using SEM, XRD, XPS, Raman spectroscopy, and UV-visible spectroscopy techniques. The reactive plasma species during the treatment processes were determined using optical emission spectroscopy. The dye degradation performance of the plasma alone and the plasma in combination with different doses of ZnO was evaluated.

2. Materials and Methods

The atmospheric pressure Ar plasma setup is like that reported in [22,23]. Briefly, AC (18 kHz), a discharge voltage of 7 kV_{pp}, was applied to a tungsten wire (diameter = 1 mm), while the other end of the wire was inserted into a quartz capillary tube with an inner diameter of 2.5 mm. An aluminum strip wound outside of the quartz tube, at 10 mm away from the edge, served as the ground electrode. Argon (99.99%), at a fixed flow rate of 3 L/min (Darhor, Hangzhou, China), was introduced into the quartz tube across the tungsten wire. The plasma was ignited inside the quartz tube and blown outward, forming a plasma plume. The discharge voltage was measured with a 1000:1 high-voltage probe (Tektronix P6015A, Tektronix, OR, USA) and monitored with a four-channel digital oscilloscope (DPO4054B, Tektronix, Beaverton, OR, USA). The composition of the plasma

spectrum was studied using an Ocean Optics USB2000 spectrometer in the spectral range of 240–900 nm.

2.1. Synthesis of ZnO Nanoparticles and Their Characterization

The ZnO nanoparticles were synthesized via hydrothermal route. All chemicals were of analytical grade and were used without further processing. Typically, 0.05 M Zinc chloride (ZnCl_2) was dissolved in 100 mL DI water under intense magnetic stirring for 1 h. During continuous stirring, 0.0028 M of C-TAB was added as a surfactant, followed by the addition 0.075 M of NaOH to maintain the pH of the reactants at 10. The solution was transferred to a hydrothermal reactor and kept in an electric furnace at a synthesis temperature of 160 °C for 5 h. Then, the hydrothermal reactor was cooled naturally to room temperature, the product was obtained through filtration, washed several times with DI water, and then dried at 60 °C in an electric furnace for 24 h. The white powder was collected for characterization and further use.

The synthesized ZnO nanoparticles were characterized using different techniques: Scanning electron microscope FE-SEM (Thermo Fisher Quanta FEG250 SEM, OR, USA) for surface morphology, X-ray diffraction XRD (Rigaku International Corp., Tokyo, Japan) for phase and crystal structure, and Raman (SENTERRA II-BRUKER, Billerica, MA, USA) spectrometer at laser wavelength 532 nm for vibrational structure. The chemical composition of ZnO was studied with X-ray photoelectron spectroscopy (XPS Thermo Scientific, Waltham, MA, USA) using a flood gun for charge compensation, while the optical properties were evaluated with a UV-5200 spectrophotometer. The pH of all samples was measured using a calibrated pH meter (model 420A, Thermo Fisher Scientific Inc.) at 25 °C.

2.2. Catalytic Performance

We investigated the catalytic performance of atmospheric pressure Ar plasma with/without (W/O) ZnO nanoparticles in the degradation of the dye methylene blue (MB) $\text{C}_{16}\text{H}_{18}\text{N}_3\text{SCl}$. An aqueous solution of MB (analytical reagent grade—Merck Germany) was prepared at a concentration of 35 mg/L. Aqueous solution of MB (30 mL) was used as the treated sample volume and placed in a beaker. To study the combined effect of plasma and a photocatalyst, we added ZnO NPs with a concentration of 0.2 and 0.4 g L^{-1} , respectively. The argon plasma orifice was placed at ~5 mm above the MB solution so that the plasma plume impinged on the solution. The degradation of the MB dye solution was evaluated by measuring their absorption spectra with an ultraviolet-visible (UV-Vis) spectrophotometer (UV-5200 Spectrophotometer, Shaanxi, China). The catalytic efficiency of the degradation of MB was calculated using [24]:

$$\text{Degradation Efficiency (\%)} = \frac{A_0 - A_t}{A_0} \times 100, \quad (1)$$

where A_0 and A_t are the absorbance of untreated MB and plasma W/O ZnO NPs treated with MB, respectively, at a given time t .

3. Results and Discussion

3.1. Optical Emission of Ar Plasma Jet

A typical emission spectrum of atmospheric pressure Ar plasma is depicted in Figure 1. The discharge parameters were at a fixed Ar flow rate of 3 L/min, discharge voltage of 7 kV_{pp} , and AC frequency of 18 KHz. The Ar plasma plume was in stable laminar Ar flow mode. The plasma emission was collected with an optical fiber facing the plasma plume. As evident from Figure 1, in addition to the Ar I line ($4p \rightarrow 4s$) in the range of 690–870 nm, other spectral bands/lines, such as at 309 nm (hydroxyl (OH)), in the 315–400 nm range (SPS of N_2 , and at 777 nm (atomic oxygen OI), can be observed. The high intensity of the Ar I spectral lines indicates the presence of high-energy electrons (≥ 11 eV), which play a crucial role in the dissociation of dye molecules. The dissociation energy of the H_2O molecule $\text{H}_2\text{O} \rightarrow \text{O} + \text{H}_2$ and/or $\text{H}_2\text{O} \rightarrow \text{OH} + \text{H}$ is 5.0 and 5.1, respectively [32,33]. In addition,

metastable argon atoms Ar* cause stepwise excitation via electron collisions, which increases plasma reactivity. The presence of OH-, N₂-, and OI-excited species are inevitable, as the Ar plasma plume is diffuse in the surrounding air; hence, energetic electrons interact with the surrounding air molecules and generate such excited species. Interestingly, Figure 1 confirms the presence of a moderately strong UV emission band (<400 nm), which induces additional pathways to generate OH radicals through ZnO nanoparticles that eventually improve the catalytic activity of the plasma-ZnO nanoparticle system.

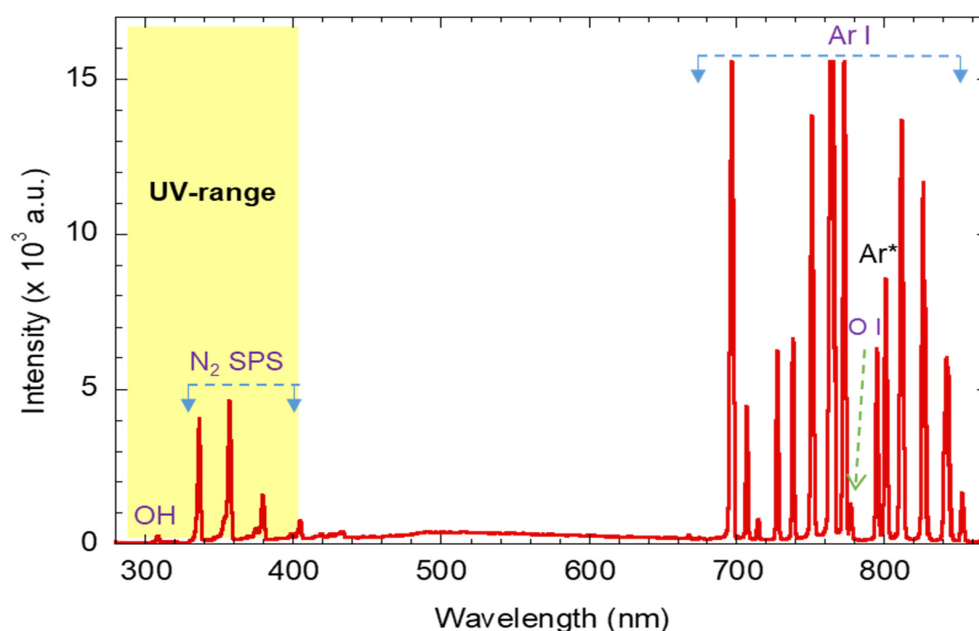


Figure 1. Typical emission spectra of the atmospheric-pressure plasma jet at Ar flow rate of 3 L/min.

3.2. Characterization of the ZnO Nanoparticles

Figure 2a shows SEM images of the synthesized ZnO nanostructures at a growth temperature of 160 °C, a pH of 10, and a synthesis time of 5 h. The SEM images show that the ZnO nanostructures have a homogeneous shape (NPs) with a diameter in the range of 30–50 nm. Furthermore, the ZnO NPs agglomerate and form nano crystallites, as shown in Figure 2a, which is like that reported in the literature [34].

Figure 2b depicts the XRD pattern of the synthesized ZnO (NPs). As observed, the pattern exhibits sharp peaks with high intensities, confirming the high crystallinity of the studied sample. The observed peaks are located at positions $2\theta = 31.72^\circ, 33.66^\circ, 36.21^\circ, 47.48^\circ, 56.51^\circ, 62.75^\circ,$ and 67.84° . The observed peaks agree well with the typical hexagonal wurtzite crystalline ZnO with space group $P63mc$ (Card No. 96-900-4180). Therefore, the diffracted peaks were labeled 100, 002, 101, 102, 110, 103, and 112. The XRD pattern of the synthesized ZnO NPs, shown in Figure 2b, displays other additional peaks at $2\theta \sim 28.6^\circ, 30.9^\circ, 32.6^\circ, 42.7^\circ,$ and 50.6° , which were assigned to Zinc oxyhydroxides Zn(OH)₂ (Card No. 96-451-7838). In other words, the synthesized ZnO NPs are composed of Zincite 99% and Zinc hydroxide (1%). The grain size D was estimated using Scherrer formula $D = \frac{0.9 \cdot \lambda}{\beta \cdot \cos \theta_B}$, where λ , β , and θ_B are the X-ray wavelength ($\lambda = 1.543 \text{ \AA}$) and the full width at half-maximum (FWHM) of the diffraction peak and the diffraction angle, respectively [32]. The strongest reflecting peak, 002, was selected to estimate the average size of ZnO. The crystallite size was about 35.05 nm, which slightly matches that observed from the SEM image. The lattice parameters a and c of the hexagonal (wurtzite) were calculated using $a = \frac{\lambda}{1.73 \cdot \sin \theta_{100}}$ and $c = \frac{\lambda}{\sin \theta_{002}}$, respectively [35]. The lattice parameters a and c were found to be 3.2533 Å and 5.2073 Å, respectively, which are comparable to the parameters of pure ZnO ($a = 3.24 \text{ \AA}, c = 5.206 \text{ \AA}$).

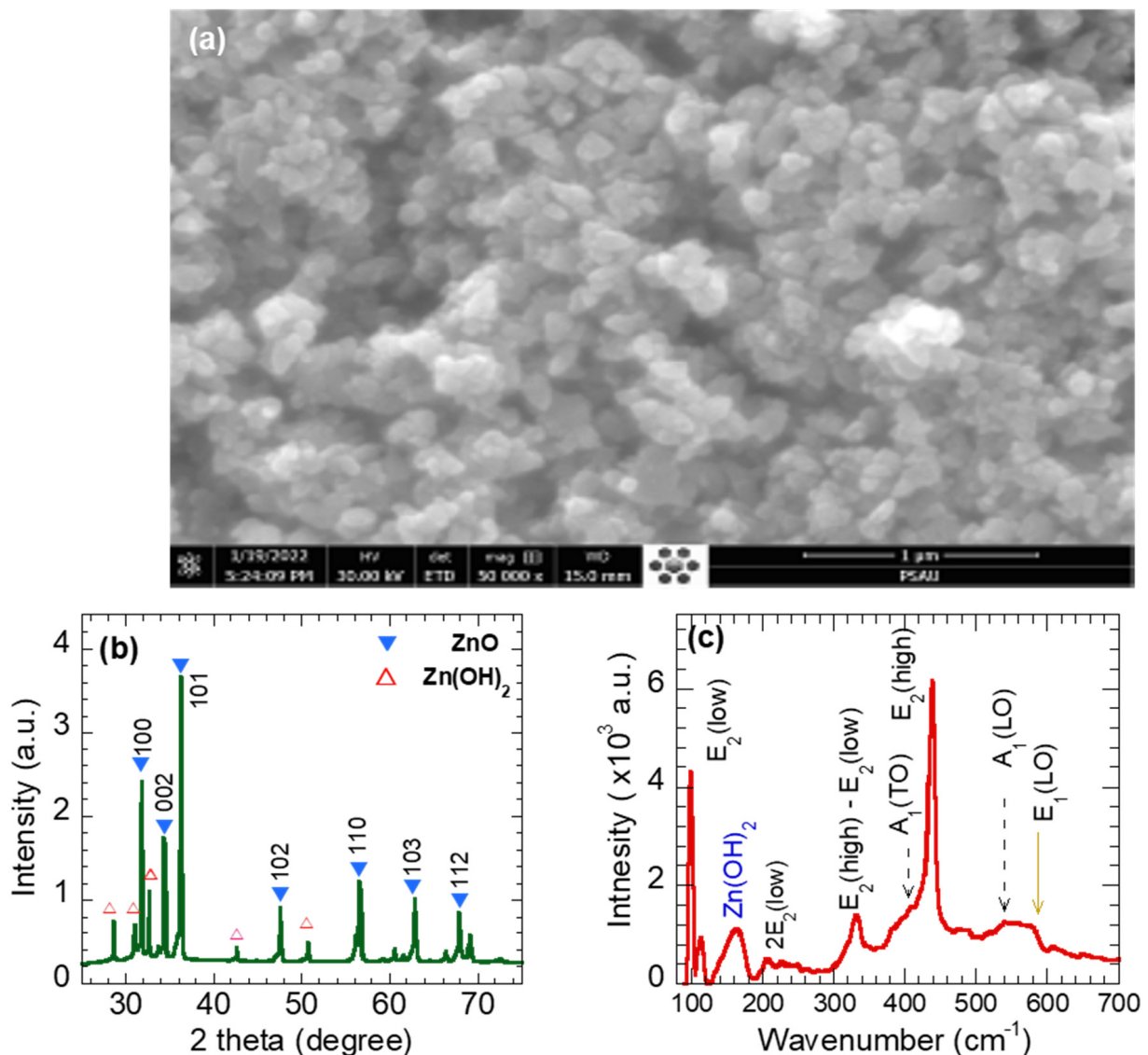


Figure 2. (a) SEM images, (b) X-ray diffraction pattern, and (c) Raman spectra of ZnO nanoparticles.

Figure 2c displays the Raman modes of a ZnO nanoparticle using a green laser $\lambda = 532$ nm at room temperature. One can observe six major peaks, located at 98.5, 210, 333, 393, 438.5, 538, and 577.5 cm^{-1} , that were assigned to modes $E_2(\text{low})$, $2E_2(\text{low})$, $E_2(\text{high})-E_2(\text{low})$, $A_1(\text{TO})$, $E_2(\text{high})$, $A_1(\text{LO})$, and $E_1(\text{LO})$, respectively [36]. The high-intensity $E_2(\text{low})$ and $E_2(\text{high})$ modes reflect the hexagonal wurtzite structure of synthesized ZnO nanoparticles [37]. The $2E_2(\text{low})$ is the second order of $E_2(\text{low})$ mode. The mode $E_2(\text{high})$, which was assigned to the oxygen vibration, is a fingerprint of the degree of crystallinity of ZnO nanoparticles, i.e., a sharp high-intensity peak indicates the high-crystalline nature of the synthesized ZnO NPs, which is consistent with the XRD result. The peak $E_1(\text{LO})$ indicates the presence of oxygen-vacancy defects [38], implying proper improvements in the ZnO NPs' photocatalysis performance. The $A_1(\text{TO})$ and $A_1(\text{LO})$ modes are first-order optical modes of wurtzite ZnO. The mode $E_2(\text{high})-E_2(\text{low})$ is a second feature of the ZnO structure. The Raman mode at ~ 160 cm^{-1} is probably attributed to $\text{Zn}(\text{OH})_2$ [39].

Figure 3a shows the XPS survey spectrum of the synthesized ZnO NPs. The apparent high-intensity $\text{Zn}2p_{3/2}$, $\text{Zn}2p_{1/2}$, and $\text{O}1s$ peaks confirm the chemical composition of the synthesized ZnO NPs, i.e., 43.8% Zn, 44.65% oxygen, and 11% carbon. The carbon content is probably contaminated during the synthesis processes. The XPS Zinc spectral lines were assigned to the Zn 3D, Zn 3p, Zn 3s, Zn LMM (Auger), and Zn 2p peaks. The oxygen line

O 1s at 530 eV was attributed to O²⁻ ions in the wurtzite ZnO structure, while Zinc spectral lines were assigned to the Zn 3D, Zn 3p, Zn 3s, Zn LMM (Auger), and Zn 2p peaks [40].

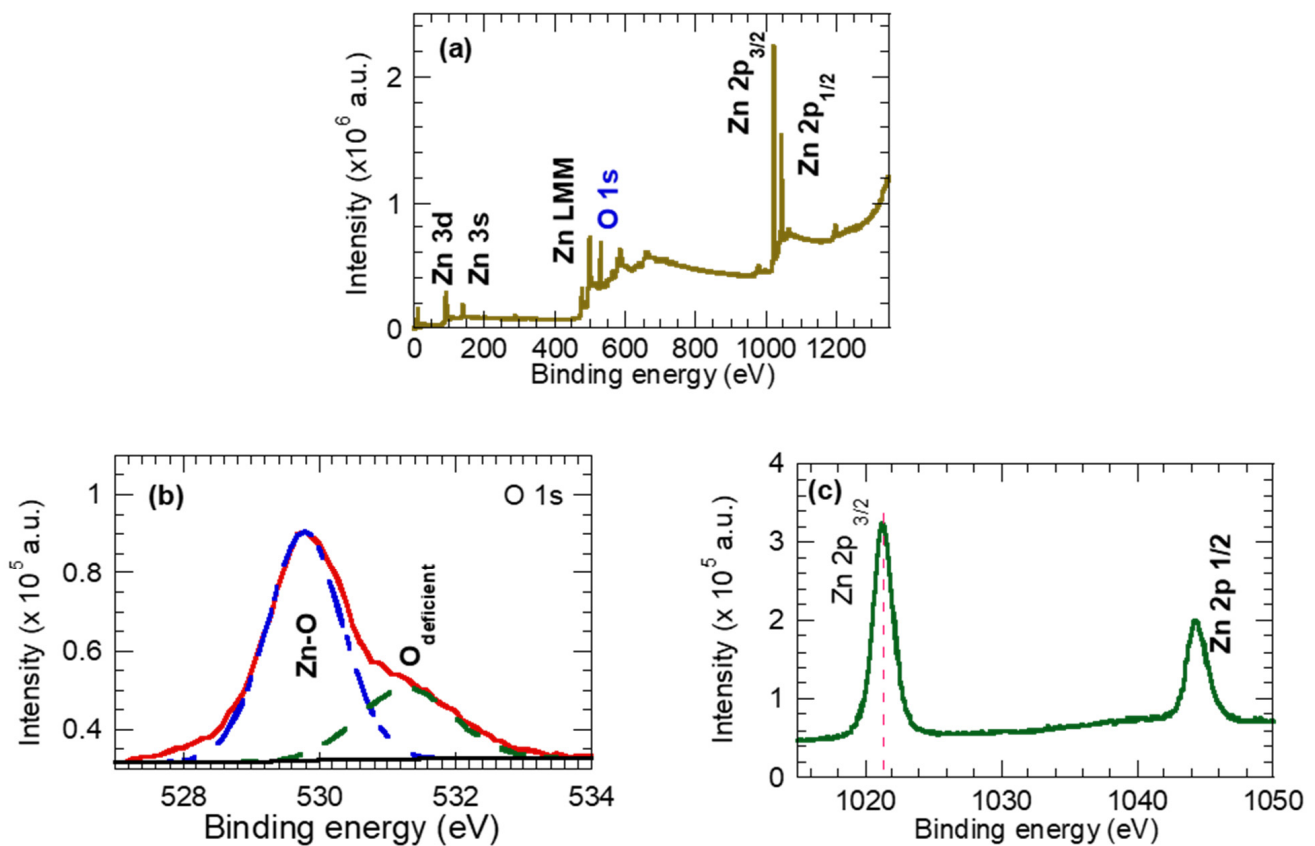


Figure 3. (a) Survey spectra ZnO nanoparticles, (b) high-resolution spectra for oxygen O1s, and (c) high-resolution spectra for Zn 2p.

To reveal the oxidation state of the Zn and O components of ZnO NPs, Figure 3b,c provide a high-resolution spectra of the O 1s and Zn2p spectral lines. The O 1s spectrum is asymmetric with a shoulder at higher binding energy, and it is decomposed into two peaks; at the lower B.E. of 530.1 eV, it is ascribed to oxygen anions O²⁻ in the wurtzite ZnO crystal lattice (Zn–O), while at a higher B.E. of 531.5 eV, it represents oxygen vacancies (V_O) [41–43] and/or OH species adsorbed on the surface of ZnO [44,45]. In fact, the XRD (Figure 2b) and Raman (Figure 2c) results support the presence of the oxygen vacancies and the OH species on the synthesized ZnO NPs. Figure 3c shows the Zn2p spectra splitting into peaks at 1021.86 eV and 1044.98 eV, which can be indexed to Zn2p_{3/2} and Zn2p_{1/2}, respectively. The Zn2p spectra corresponds to the Zn atom at the regular lattice site in ZnO. Here, the binding energy separation between the Zn2p_{3/2} and Zn2p_{1/2} peaks was found to be 23.06 eV, which is consistent with the emissions from Zn²⁺ ions in the ZnO crystal.

Figure 4a displays the UV-Vis absorption spectrum of ZnO NPs. The spectrum exhibits strong absorption in the UV range < 400 nm, with the absorption peak at 366 nm assigned to the intrinsic band-gap absorption of ZnO [46]. The absorption peak at 366 nm is a characteristic of the hexagonal wurtzite ZnO structure. Further, ZnO NPs' UV-Vis spectrum reveals a blue shift compared with defect-free ZnO (368 nm) [47,48], probably due to the quantum size effect.

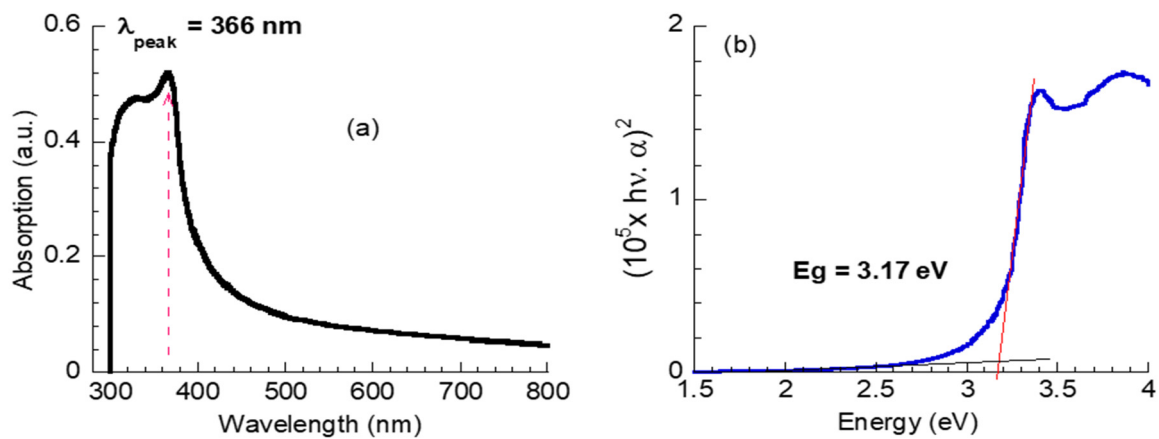


Figure 4. (a) UV-visible optical absorption, (b) plots of $(hv\alpha)^2$ versus hv of ZnO nanoparticles.

The optical direct band gap energy, E_g , for the synthesized ZnO NPs was estimated using Tauc law [49],

$$hv \cdot \alpha = A \cdot (hv - E_g)^n$$

where α is the absorption coefficient, hv is the photon energy, A is constant, and $n = 1/2$ for the direct band gap. The E_g value was obtained via an extrapolation of the linear part of the $(hv\alpha)^2$ versus hv to $hv\alpha = 0$. The value of α was computed from the absorption spectrum. As seen in Figure 4b, the E_g value was 3.17 eV, which is smaller than the defect-free bulk ZnO ($E_g = 3.3 \text{ eV}$) [50]. The decrease in the E_g value is probably attributed to the formation of a shallow level within the band gap due to the presence of some defects in ZnO NPs, such as the oxygen vacancies as observed in the O 1s spectrum of the XPS results, as shown in Figure 3b, and the attached hydroxyl as observed in the XRD and Raman results.

4. Catalysis Performance

The catalytic performance of atmospheric argon plasma W/O ZnO NPs has been evaluated from the MB absorption spectra. The absorbance spectra of the MB dye solution treated with Ar plasma W/O ZnO NPs at different treatment-time values are presented in Figure 5a–c. As evident, the absorption spectra of pristine MB dye solutions (Figure 5a) have a characteristic absorption peak at 663 nm associated with an MB monomer, and a shoulder at a lower wavenumber of 616 nm assigned to the MB dimer. The intensity of the peak at 663 nm is proportional to the concentration of the undissociated MB dye molecules in the solution sample. After exposure to the Ar plasma W/O ZnO NPs, the overall MB absorption intensity decreases, as shown in Figure 5a–c. In particular, the peak intensity at 663 nm dramatically decreases, implying the degradation of the chromophore group in MB molecules [50]. The wavelength at which the MB absorption peak is located (663 nm) is related to the length of the conjugated systems in the MB molecule [51]. Figure 5d shows the position of the MB absorption peak as a function of treatment time for the Ar plasma W/O ZnO NPs' treatment processes as it clears the peak shifts to a lower value (blue shift), particularly during the Ar plasma "alone" treatment. This behavior is attributed to the destroying of the conjugated system of MB and the formation of by-products such as Azure and Thionine [52] through the demethylation/degradation of MB during the treatment process [53]. The pH value of the pristine MB was slightly acidic at 5.4 and turned to be neutral with a pH of 6, 6.33, and 6.5 for the samples treated with Ar plasma and Ar plasma combined with 0.2 and 0.4 gL^{-1} ZnO, respectively. Knowing that, plasma increased the acidity of the exposure DI water [54]; the increases in the pH values of plasma-treated MB solutions imply physiochemical changes in the treated solution, which is consistent with the shift observed in the MB absorption peak.

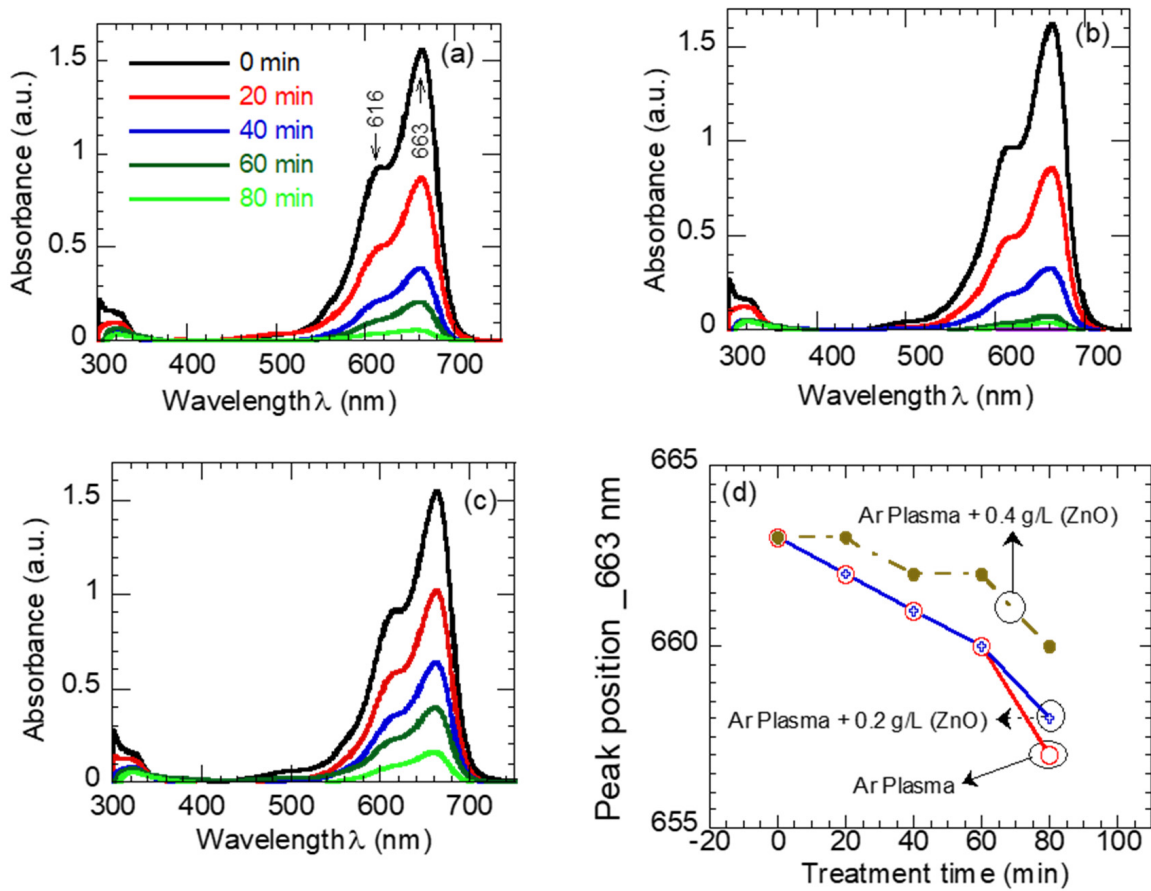


Figure 5. Absorption spectra of MB dye (a) sole plasma exposure, (b) plasma + 0.2 gL⁻¹ ZnO, (c) plasma + 0.4 gL⁻¹ ZnO solution mixture, and (d) the position of the MB absorption peaks as a function of exposure time.

To quantify the photocatalytic performance of Ar plasma W/O ZnO NPs, the degradation efficiency was calculated from Equation (1), and the results are depicted in Figure 6. The rate of MB degradation was found to depend on the presence of ZnO NPs as well as the concentration of ZnO NPs. For example, the degradation efficiency after 60 min of treatment was found to be 86% (plasma alone), 95% (plasma combined with 0.2 gL⁻¹ of ZnO), and 74% (plasma combined with 0.4 gL⁻¹ of ZnO).

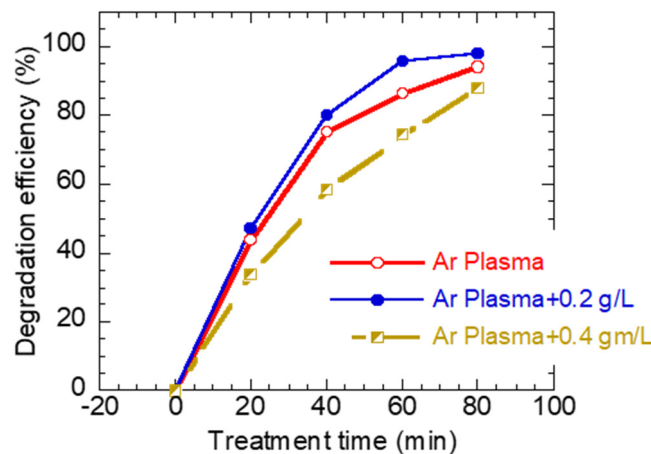


Figure 6. The degradation efficiency of MB dye as a function of exposure time for (a) plasma “alone” exposure, (b) plasma + 0.2 gL⁻¹ ZnO, and (c) plasma + 0.4 gL⁻¹ ZnO solution mixture.

The mechanism of MB degradation is illustrated in Figure 7 and can be explained as follows.

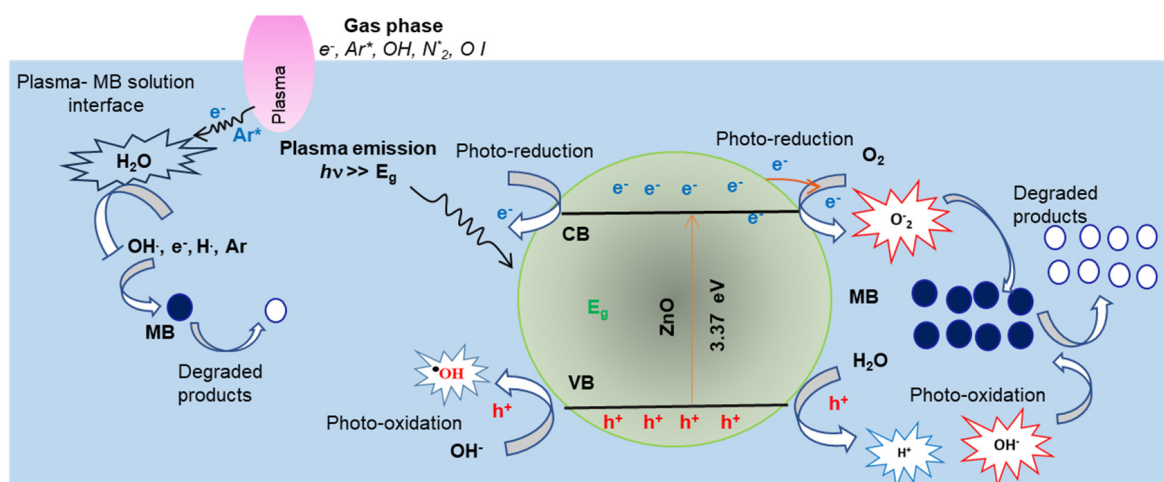
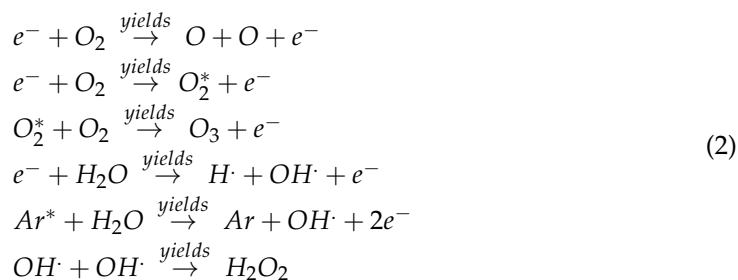


Figure 7. Schematic diagram of the effects of plasma and ZnO NP photocatalysis reaction pathways for MB degradation.

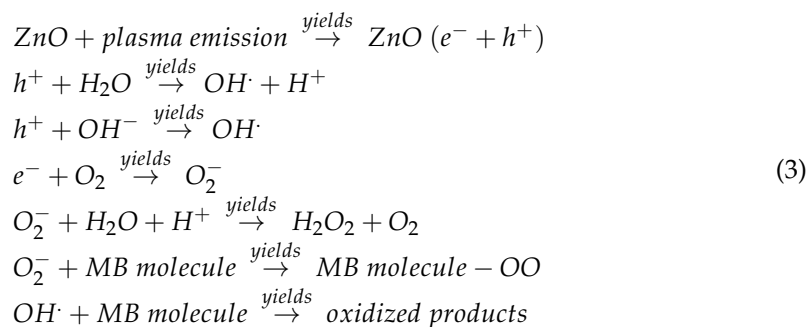
Considering the plasma emission and the subsequent chemical reactions taking place at the Ar plasma–MB solution interface, the OES measurements (Figure 1) confirm the existences of OH·, N₂·, and OI· reactive radicals. In addition, the emitted Ar I lines imply the presence of high-energy electrons >> 11 eV and the Ar metastable A* species. The dissociation energy of H₂O molecules into OH·, H₂, and O· are 5.0–5.1 eV [32,33]. Hence, one would expect various interaction pathways between plasma active species and the surrounding air (gas phase), as well as at the plasma–water interface. Some examples of possible reaction pathways [55,56] are listed in Equation (2)



The generated species moved with the Ar flow to the plasma–liquid interface, diffused in the MB solution, and played crucial roles in the degradation of the MB dye molecules. The oxidation potential of the OH· (Hydroxyl radical), O·, O₃ (Ozone), and H₂O₂ (Hydrogen peroxide) species are 2.8, 2.42, 2.07, and 1.77, respectively. Hence, OH· was found to be the main oxidative species in the plasma “alone” water treatment [57]. For instance, the OH· radicals in the MB aqueous solutions absorbed electrons from the double bonds of methylene blue molecules, leading to the degradation of the MB solution [58]. Further, the high-energy electrons interacted with MB molecules, removing the methyl group (CH₃) via demethylation [59].

As shown, the availability of OH· radicals determine the efficiency of the MB degradation process. Hence the addition of OH· source radicals combined with that generated with plasma would improve the degradation of MB dye. Indeed, the MB degradation improved in the presence of the 0.2 gL⁻¹ ZnO photocatalyst in the MB solution, as shown in Figure 6. As depicted in Figure 1, the plasma emission contains UV photons << 400 nm), which have enough energy to activate ZnO photocatalysts; electrons (e⁻) move from the valence band (VB) to the conduction band (CB) and leave holes h⁺ in the (VB) of ZnO NPs.

Both e^- and h^+ migrate to the ZnO NPs' surface. The holes' h^+ oxidizes H_2O and/or OH^- molecules are adsorbed on the ZnO NPs' surface and produce reactive hydroxyl radical anions (OH^\cdot) and H^+ ions. Meanwhile, electrons reduced to oxygen molecules O_2 exist on the photocatalyst surface and generate super-oxide anions ($\cdot O_2^-$) [60–63]. The O_2^- might interact with H^+ in the presence of H_2O and generate H_2O_2 . In addition, oxygen vacancies in the ZnO NPs (Figure 3b) act as electron e^- donors that promote further generation of OH^\cdot . The reactive OH^\cdot and O_2^- oxidize the MB dye molecules into de-colored harmless species. The possible reaction pathways for MB degradation in the presence of ZnO NPs under plasma irradiation are summarized in the following equations.



Surprisingly, when the amount of the photocatalyst (ZnO NPs) increased from 0.2 to 0.4 gL⁻¹, the MB degradation efficiency slightly decreased, as shown in Figure 5. The increase in ZnO NPs might induce turbidity in the MB solution, which would decrease the number of UV photons reaching the ZnO NPs' surface, leading to less generation of $e^-—h^+$ pairs and, hence, lower OH^\cdot radicals generated and a decrease in the degradation efficiency. Alternatively, the synthesized ZnO NPs contain some ZnO (OH)₂, i.e., an OH group, attached to the ZnO's surface. Hence, the increase in ZnO NPs increases the number of OH groups which might participate in other surface reactions that compete with the catalytic reactions, potentially reducing the overall catalytic activity. This is why a slight decrease in the degradation rate was observed with a higher content of ZnO NPs (0.4 gL⁻¹).

5. Conclusions

In summary, this study investigated the synergetic effect of an atmospheric-pressure plasma treatment and the photocatalytic activity of synthesized ZnO nanoparticles on the degradation of methylene blue dye. Therefore, the first part of this paper presented the synthesis of ZnO nanoparticles using the hydrothermal route, and their physicochemical characteristics were assessed via SEM, XRD, Raman, XPS, and UV-visible techniques. The synthesized ZnO had nanoparticles with a size of 30–50 nm, was crystallite with a hexagonal lattice structure, and the $E_g = 3.17$ eV. The atmospheric-pressure plasma was generated at a fixed discharge voltage and flow rate. Reactive species, such as excited/metastable Ar, hydroxyl (OH), N_2^* , and atomic oxygen OI, could be detected via optical emission spectroscopy. The plasma treated methylene blue remotely; the plasma species interacted with the surrounding air, generated various radicals diffused in the MB solution, and played a crucial role in the degradation of the MB dye. Adding ZnO nanoparticles to the MB solution under plasma treatment influenced the plasma degradation efficiency; the MB degradation efficiency of plasma improved in the presence of 0.2 gL⁻¹ ZnO, while it decreased when the loading ZnO increased to 0.4 gL⁻¹ ZnO. The improvements in plasma performance in the case of 0.2 gL⁻¹ ZnO were probably due to the increased generation of OH^\cdot radicals, while the higher 0.4 gL⁻¹ ZnO probably caused turbidity in the MB solution and, hence, limited UV-photons and other plasma species reaching the ZnO NP surface.

Author Contributions: E.A.-F. fabricated the plasma jet and performed OES measurements; E.A.-F. and S.A. conducted experiments and analysis. E.A.-F. wrote the paper; S.A. reviewed the draft; E.A.-F. secured the funding for project. All authors have read and agreed to the published version of the manuscript.

Funding: This research was funded by the deanship of scientific research at Prince Sattam Bin Abdulaziz University, grant number (PSAU-2022/01/22237).

Institutional Review Board Statement: Not applicable.

Informed Consent Statement: Not applicable.

Data Availability Statement: The data that support the findings of this study are available on request from the corresponding author.

Conflicts of Interest: The authors declare that they have no known competing financial interests or personal relationships that could have appeared to influence the work reported in this paper.

References

1. Garg, A.; Chopra, L. Dye Waste: A significant environmental hazard. *Mater. Today Proc.* **2022**, *48*, 1310–1315.
2. Alsukaibi, A.K.D. Various Approaches for the Detoxification of Toxic Dyes in Wastewater. *Processes* **2022**, *10*, 1968. [[CrossRef](#)]
3. Ben Slama, H.; Bouket, A.C.; Pourhassan, Z.; Alenezi, F.N.; Silini, A.; Cherif-Silini, H.; Oszako, T.; Luptakova, L.; Golinska, P.; Belbahri, L. Diversity of Synthetic Dyes from Textile Industries, Discharge Impacts and Treatment Methods. *Appl. Sci.* **2021**, *11*, 6255. [[CrossRef](#)]
4. Lellis, B.; Fávaro-Polonio, C.Z.; Pamphile, J.A.; Polonio, J.C. Effects of textile dyes on health and the environment and bioremediation potential of living organisms. *Biotechnol. Res. Innov.* **2019**, *3*, 275–290.
5. Khan, I.; Saeed, K.; Zekker, I.; Zhang, B.; Hendi, A.H.; Ahmad, A.; Ahmad, S.; Zada, N.; Ahmad, H.; Shah, L.A.; et al. Review on Methylene Blue: Its Properties, Uses, Toxicity and Photodegradation. *Water* **2022**, *14*, 242. [[CrossRef](#)]
6. Al-Tohamy, R.; Ali, S.; Li, F.; Okasha, K.M.; Mahmoud, Y.A.-G.; Elsamahy, T.; Jiao, H.; Fu, Y.; Sun, J. A critical review on the treatment of dye-containing wastewater: Ecotoxicological and health concerns of textile dyes and possible remediation approaches for environmental safety. *Ecotoxicol. Environ. Saf.* **2022**, *231*, 113160. [[PubMed](#)]
7. Bhavya, G.; Belorkar, S.A.; Mythili, R.; Geetha, N.; Shetty, H.S.; Udikeri, S.S.; Jogaiah, S. Remediation of emerging environmental pollutants: A review based on advances in the uses of eco-friendly biofabricated nanomaterials. *Chemosphere* **2021**, *275*, 129975.
8. Kouchakpour, F.; Chaibakhsh, N.; Naeemi, A.S. Efficient removal of cytotoxic drugs from wastewater by single-stage combined photocatalysis–algae treatment process. *Environ. Technol.* **2021**, *42*, 3178–3190.
9. Guo, Y.; Zhao, E.; Wang, J.; Zhang, X.; Huang, H.; Yu, G.; Wang, Y. Comparison of emerging contaminant abatement by conventional ozonation, catalytic ozonation, O₃/H₂O₂ and electro-peroxone processes. *J. Hazard. Mater.* **2020**, *389*, 121829.
10. Baral, A.; Das, D.P.; Minakshi, M.; Ghosh, M.K.; Padhi, D.K. Probing Environmental Remediation of RhB Organic Dye Using a-MnO₂ under Visible- Light Irradiation: Structural, Photocatalytic and Mineralization Studies. *ChemistrySelect* **2016**, *1*, 4277–4285.
11. Pham, V.H.T.; Kim, J.; Chang, S.; Chung, W. Biodegradation of Methylene Blue Using a Novel Lignin Peroxidase Enzyme Producing Bacteria, Named *Bacillus* sp. React3, as a Promising Candidate for Dye-Contaminated Wastewater Treatment. *Fermentation* **2022**, *8*, 190. [[CrossRef](#)]
12. Fu, Y.; Viraraghavan, T. Fungal decolorization of dye wastewaters: A review. *Bioresour. Technol.* **2002**, *79*, 251–262.
13. Zhang, Z.; Kim, C.; Fernandez, C.; Sundaram, M.M.; Ramakrishnappa, T.; Wang, Y.; Wang, L.; Sun, T.; Hu, X. Adsorption removal of methylene blue from aqueous solution on carbon coated Fe₃O₄ microspheres functionalized with chloroacetic acid. *Sci. Eng. Compos. Mater.* **2018**, *25*, 353–361.
14. Mohammed, M.A.; Shitu, A.; Ibrahim, A. Removal of Methylene Blue Using Low Cost Adsorbent: A Review. *Res. J. Chem. Sci.* **2014**, *4*, 91–102.
15. Parakala, S.; Moulik, S.; Sridhar, S. Effective separation of methylene blue dye from aqueous solutions by integration of micellar enhanced ultrafiltration with vacuum membrane distillation. *Chem. Eng. J.* **2019**, *375*, 122015.
16. Robinson, T.; McMullan, G.; Marchant, R.; Nigam, P. Remediation of dyes in textile effluent: A critical review on current treatment technologies with a proposed alternative. *Bioresour. Technol.* **2001**, *77*, 247–255.
17. Hou, C.; Hu, B.; Zhu, J. Photocatalytic Degradation of Methylene Blue over TiO₂ Pretreated with Varying Concentrations of NaOH. *Catalysts* **2018**, *8*, 575–587.
18. Dutta, K.; Mukhopadhyay, S.; Bhattacharjee, S.; Chaudhuri, B. Chemical oxidation of methylene blue using a Fenton-like reaction. *J. Hazard. Mater.* **2001**, *84*, 57–71.
19. Sultan, T.; Cho, J. Optimization of a UV- H₂O₂ AOP System Using Scavenger Radicals and Response Surface Methodology. *Chem. Eng. Commun.* **2016**, *203*, 1093–1104.
20. Abdel-Fattah, E.; Ogawa, D.; Nakamura, K. Oxygen functionalization of MWCNTs in RF-dielectric barrier discharge Ar/O₂ plasma. *J. Phys. D Appl. Phys.* **2017**, *50*, 265301.

21. Abdel-Fattah, E. Surface and thermal characteristics relationship of atmospheric pressure plasma treated natural luffa fibers. *Eur. Phys. J. D* **2019**, *73*, 71. [[CrossRef](#)]
22. Abdel-Fattah, E. Surface Activation of Poly(Methyl Methacrylate) with Atmospheric Pressure Ar + H₂O Plasma. *Coatings* **2019**, *9*, 228. [[CrossRef](#)]
23. Abdel-Fattah, E. Polyimide Surface Modification Using He-H₂O Atmospheric Pressure Plasma Jet-Discharge Power Effect. *Coatings* **2020**, *10*, 662. [[CrossRef](#)]
24. Abdel-Fattah, E. Atmospheric pressure helium plasma jet and its applications to methylene blue degradation. *J. Electrostat.* **2019**, *101*, 103360. [[CrossRef](#)]
25. Lin, Y.-C.; Liang, F.-Y.; Fu, C.-K.; Chang, K.L. Removal of Isopropanol by synergistic non-thermal plasma and photocatalyst. *J. Hazard. Mater.* **2022**, *424*, 126874. [[CrossRef](#)] [[PubMed](#)]
26. Jia, Z.; Wang, X.; Emeric Foucher, E.; Thevenet, F.; Rousseau, A. Plasma-Catalytic Mineralization of Toluene Adsorbed on CeO₂. *Catalysts* **2018**, *8*, 303. [[CrossRef](#)]
27. Rong, X.; Cao, Q.; Gao, Y.; Luan, T.; Li, Y.; Man, Q.; Zhang, Z.; Chen, B. Synergistic Catalytic Performance of Toluene Degradation Based on Non-Thermal Plasma and Mn/Ce-Based Bimetal-Organic Frameworks. *Molecules* **2022**, *27*, 7363. [[CrossRef](#)]
28. Jung, S.-C.; Lee, H.; Ki, S.J.; Kim, S.-J.; Park, Y.-K. Rapid decomposition of chloroform by a liquid phase plasma reaction with titanium dioxide and hydrogen peroxide. *Catal. Today* **2020**, *352*, 54–59. [[CrossRef](#)]
29. Ghezzer, M.R.; Ognier, S.; Cavadias, S.; Abdelmalek, F.; Addou, A. DBD plate-TiO₂ treatment of Yellow Tartrazine azo dye solution in falling film. *Sep. Purif. Technol.* **2013**, *104*, 250–255. [[CrossRef](#)]
30. Pandiyaraj, K.N.; Vasu, D.; Ghobeira, R.; Tabaei, P.S.E.; De Geyter, N.; Morent, R.; Pichumani, M.; Padmanabhanan, P.V.A.; Deshmukh, R.R. Dye wastewater degradation by the synergetic effect of an atmospheric pressure plasma treatment and the photocatalytic activity of plasma-functionalized Cu-TiO₂ nanoparticles. *J. Hazard. Mater.* **2021**, *405*, 124264. [[CrossRef](#)]
31. Mohamed, K.M.; Benitto, J.J.; Vijaya, J.J.; Bououdina, M. Recent Advances in ZnO-Based Nanostructures for the Photocatalytic Degradation of Hazardous, Non-Biodegradable Medicines. *Crystals* **2023**, *13*, 329. [[CrossRef](#)]
32. Itikawa, Y.; Mason, N.J. Cross Sections for Electron Collisions with Water Molecules. *Phys. Chem. Ref. Data* **2005**, *34*, 1–22. [[CrossRef](#)]
33. Luo, Y.R.; Cheng, J.P. *Bond Dissociation Energies in CRC Handbook of Chemistry and Physics*, 92nd ed.; CRC Press: Boca Raton, FL, USA, 2011.
34. Minakshi, M.; Appadoo, D.; Martin, D.E. The Anodic Behavior of Planar and Porous Zinc Electrodes in Alkaline Electrolyte. *Electrochem. Solid-State Lett.* **2010**, *13*, A77–A80. [[CrossRef](#)]
35. Bindu, P.; Thomas, S. Estimation of lattice strain in ZnO nanoparticles: X-ray peak profile analysis. *J. Theor. Appl. Phys.* **2014**, *8*, 123–134. [[CrossRef](#)]
36. Zhang, L.; Zhao, J.; Zheng, J.; Li, L.; Zhu, Z. Shuttle-like ZnO nano/microrods: Facile synthesis, optical characterization and high formaldehyde sensing properties. *Appl. Surf. Sci.* **2011**, *258*, 711–718. [[CrossRef](#)]
37. Arguello, C.A.; Rousseau, D.L.; Porto, S.P.S. First-Order Raman Effect in Wurtzite-Type Crystals. *Phys. Rev.* **1969**, *181*, 1351–1363. [[CrossRef](#)]
38. Li, J.Y.; Li, H. Physical and electrical performance of vapor-solid grown ZnO straight nanowires. *Nanoscale Res. Lett.* **2009**, *4*, 165–168. [[CrossRef](#)]
39. Wang, M.; Jiang, L.; Kim, E.J.; Hahn, S.H. Electronic structure and optical properties of Zn(OH)₂: LDA+U calculations and intense yellow luminescence. *RSC Adv.* **2015**, *5*, 87496. [[CrossRef](#)]
40. Beamson, G.; Briggs, D. *High Resolution XPS of Organic Polymers: The Scienta ESCA300 Database*; John Wiley and Sons: Chichester, UK, 1992.
41. Wang, Z.G.; Zu, X.T.; Zhub, S.; Wang, L.M. Green luminescence originates from surface defects in ZnO nanoparticles. *Phys. E* **2006**, *35*, 199–202. [[CrossRef](#)]
42. Sahai, A.; Goswami, N. Probing the dominance of interstitial oxygen defects in ZnO nanoparticles through structural and optical characterizations. *Ceram. Int.* **2014**, *40*, 14569–14578. [[CrossRef](#)]
43. Ramgir, N.S.; Late, D.J.; Bhise, A.B.; More, M.A.; Mulla, I.S.; Joag, D.S.; Vijayamohan, K. ZnO multipods, submicron wires, and spherical structures and their unique field emission behavior. *J. Phys Chem. B* **2006**, *110*, 18236. [[CrossRef](#)]
44. Heinhold, R.; Williams, G.T.; Cooil, S.P.; Evans, D.A.; Allen, M.W. Influence of polarity and hydroxyl termination on the band bending at ZnO surfaces. *Phys. Rev. B* **2013**, *88*, 235315. [[CrossRef](#)]
45. Coppa, B.J.; Fulton, C.C.; Kiesel, S.M.; Davis, R.F.; Pandarinath, C.; Burnette, J.E.; Nemanich, R.J.; Smith, D.J. Structural, microstructural, and electrical properties of gold films and Schottky contacts on remote plasma-cleaned, *n*-type ZnO(0001) surfaces. *J. Appl. Phys.* **2005**, *97*, 103517. [[CrossRef](#)]
46. Zak, A.K.; Abrishami, M.E.; Majid, W.A.; Yousefi, R.; Hosseini, S. Effects of annealing temperature on some structural and optical properties of ZnO nanoparticles prepared by a modified sol-gel combustion method. *Ceram. Int.* **2011**, *37*, 393–398. [[CrossRef](#)]
47. Berger, L.I. *Semiconductor Materials*; CRC Press: Boca Raton, FL, USA, 1997.
48. Sun, J.H.; Dong, S.Y.; Feng, J.L.; Yin, X.-J.; Zhao, X.C. Enhanced sunlight photocatalytic performance of Sn-doped ZnO for Methylene Blue degradation. *J. Mol. Catal. A* **2011**, *335*, 145. [[CrossRef](#)]
49. Tauc, J.; Grigorovici, R.; Vancu, A. Optical Properties and Electronic Structure of Amorphous Germanium. *Phys. Status Solidi. B* **1966**, *15*, 627–637. [[CrossRef](#)]

50. Tang, S.; Wang, Z.; Yuan, D.; Zhang, Y.; Qi, J.; Rao, Y.; Lu, G.; Li, B.; Wang, K.; Yin, K. Enhanced photocatalytic performance of BiVO₄ for degradation of methylene blue under LED visible light irradiation assisted by peroxymonosulfate. *Int. J. Electrochem. Sci.* **2020**, *15*, 2470–2480. [[CrossRef](#)]
51. Dyer, J.R. *Applications of Absorption Spectroscopy of Organic Compounds*; Prentice-Hall: Hoboken, NJ, USA, 1965; p. 19.
52. Antoniadou, M.; Arfanis, M.K.; Ibrahim, I.; Falaras, P. Bifunctional g-C₃N₄/WO₃ thin films for photocatalytic water purification. *Water* **2019**, *11*, 2439. [[CrossRef](#)]
53. Rauf, M.A.; Meetani, M.A.; Khaleel, A.; Ahmed, A. Photocatalytic degradation of Methylene Blue using a mixed catalyst and product analysis by LC/MS. *Chem. Eng. J.* **2010**, *157*, 373–378. [[CrossRef](#)]
54. Thirumdas, R.; Kothakota, A.; Annapure, U.; Siliveru, K.; Blundell, R.; Gatt, R.; Valdramidis, V.P. Plasma activated water (PAW): Chemistry, physico-chemical properties, applications in food and agriculture. *Trends Food Sci. Technol.* **2018**, *77*, 21–31. [[CrossRef](#)]
55. Xiong, R.; Nikiforov, A.; Vanraes, P.; Leys, C. Hydrogen peroxide generation by dc and pulsed underwater discharge in air bubbles. *J. Adv. Oxid. Technol.* **2012**, *15*, 197–204. [[CrossRef](#)]
56. Reddy, P.M.K.; Raju, B.R.; Karuppiyah, J.; Reddy, E.L.; Subrahmanyam, C. Degradation and mineralization of methylene blue by dielectric barrier discharge non-thermal plasma reactor. *Chem. Eng. J.* **2013**, *217*, 41–47. [[CrossRef](#)]
57. Dai, F.; Fan, X.; Stratton, G.R.; Bellona, C.L.; Holsen, T.M.; Crimmins, B.S.; Xia, X.; Mededovic, T.S. Experimental and density functional theoretical study of the effects of Fenton's reaction on the degradation of Bisphenol A in a high voltage plasma reactor. *J. Hazard. Mater.* **2016**, *308*, 419–429. [[CrossRef](#)]
58. Maehara, T.; Toyota, H.; Kuramoto, M.; Iwamae, A.; Tadokoro, A.; Mukasa, S.; Yamashita, H.A.; Kawashima, A.; Nonura, S. Radio Frequency Plasma in Water. *Jpn. J. Appl. Phys.* **2006**, *45*, 8864. [[CrossRef](#)]
59. Wu, L.; Xie, Q.; Lv, Y.; Wu, Z.; Liang, X.; Lu, M.; Nie, Y. Degradation of Methylene Blue via Dielectric Barrier Discharge Plasma Treatment. *Water* **2019**, *11*, 1818. [[CrossRef](#)]
60. Liu, Z.; Song, Y.; Wang, Q.; Jia, Y.; Tan, X.; Du, X.; Gao, S. Solvothermal fabrication and construction of highly photoelectrocatalytic TiO₂ NTs/Bi₂MoO₆ heterojunction based on titanium mesh. *J. Colloid Interface Sci.* **2019**, *556*, 92–101. [[CrossRef](#)]
61. Wang, Q.; Li, H.; Yu, X.; Jia, Y.; Chang, Y.; Gao, S. Morphology regulated Bi₂WO₆ nanoparticles on TiO₂ nanotubes by solvothermal Sb³⁺ doping as effective photocatalysts for wastewater treatment. *Electrochim. Acta* **2020**, *330*, 135167. [[CrossRef](#)]
62. Yao Jia, Y.; Liu, P.; Wang, Q.; Wu, Y.; Cao, D.; Qiao, Q.-A. Construction of Bi₂S₃-BiOBr nanosheets on TiO₂ NTA as the effective photocatalysts: Pollutant removal, photoelectric conversion, and hydrogen generation. *J. Colloid Interface Sci.* **2021**, *585*, 459–469. [[CrossRef](#)]
63. Wang, Q.; Zhu, S.; Zhao, S.; Li, C.; Wang, R.; Cao, D.; Li, G. Construction of Bi-assisted modified CdS/TiO₂ nanotube arrays with ternary S-scheme heterojunction for photocatalytic wastewater treatment and hydrogen production. *Fuel* **2022**, *322*, 124163. [[CrossRef](#)]

Disclaimer/Publisher's Note: The statements, opinions and data contained in all publications are solely those of the individual author(s) and contributor(s) and not of MDPI and/or the editor(s). MDPI and/or the editor(s) disclaim responsibility for any injury to people or property resulting from any ideas, methods, instructions or products referred to in the content.